

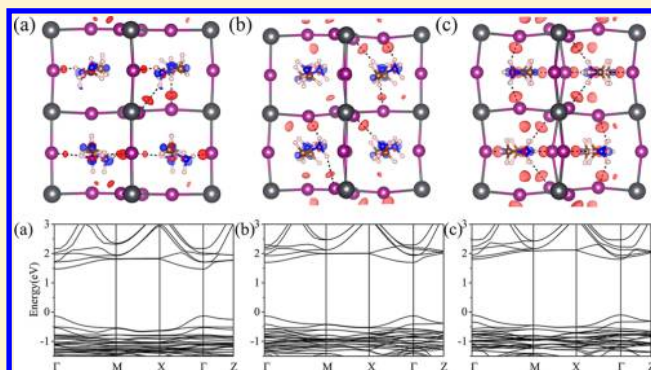
First-Principles Study of Lead Iodide Perovskite Tetragonal and Orthorhombic Phases for Photovoltaics

Wei Geng,[†] Le Zhang,[†] Yan-Ning Zhang,^{†,‡} Woon-Ming Lau,^{†,‡} and Li-Min Liu^{*,†}

[†]Beijing Computational Science Research Center, 3 Heqing Street, Haidian District, Beijing 100084, China

[‡]Chengdu Green Energy and Green Manufacturing Technology R&D Center, Chengdu, Sichuan 610207, China

ABSTRACT: Methylammonium lead iodide perovskite, $\text{CH}_3\text{NH}_3\text{PbI}_3$, has attracted particular attention because of its fast increase in efficiency as solid-state solar cells. We performed first-principles calculations with the nonlocal van der Waals (vdW) correlation to investigate the crystal structures and electronic and optical properties of $\text{CH}_3\text{NH}_3\text{PbI}_3$. The calculated results show that the distribution of methylammonium ions, which further changes the vdW interaction and hydrogen bonds of organic and inorganic matrixes, plays a vital role in both the geometry stability and the electronic structure. The vdW correlation is critical to provide appropriate descriptions of the interaction between the organic and the inorganic parts. The phase transformation from orthorhombic to tetragonal phase causes the decrease of the band gap and the red shift of the optical absorption coefficient.



1. INTRODUCTION

Dye-sensitized solar cells (DSCs) based on nanocrystalline TiO_2 are a promising photovoltaic device for a renewable energy source because of their easy fabrication, low cost, and flexibility.^{1,2} The light-harvesting molecular dyes in an organic solvent is widely used as the TiO_2 sensitizer.³ However, the liquid electrolytes lead to several technological problems, such as dye degradation, solvent evaporation, and leakage of the solvent, which greatly limit the stability of the DSC device for photovoltaic applications. Currently, many efforts have been made to search for new solid hole transport materials so as to replace liquid electrolytes and get solid-state dye-sensitized solar cells (ssDSCs) with good stability and high efficiency.^{4–8}

Methylammonium lead iodide perovskite ($\text{CH}_3\text{NH}_3\text{PbI}_3$), which was proposed by Miyasaka et al., is considered as a promising material for ssDSCs with an expected photo-conversion efficiency of 20%.^{9–11} $\text{CH}_3\text{NH}_3\text{PbI}_3$ was first used as sensitizing materials in liquid DSCs in 2009, with a very low power conversion efficiency (PCE) of 3.8%.^{12,13} In 2012, Chung et al. introduced a related inorganic CsSnI_3 perovskite in ssDSCs as hole conduction, in the presence of ruthenium dye N719, and the ssDSCs showed a 8.5% efficiency.¹⁴ In the same year, Kim et al. used spiro-MeOTAD based perovskite ssDSCs to reach a high photovoltaic efficiency of 9.7%.¹⁵ Recently, researches of perovskite-based solar cells steeply increased and an impressive efficiency value of up to 15% was reported in 2013.^{16,17}

The extremely fast progress in perovskite photovoltaic materials has attracted increasing attention, both experimentally and theoretically. Many theoretical efforts have been performed on the structural, electronic, and optical properties of

$\text{CH}_3\text{NH}_3\text{PbI}_3$ perovskite based on density functional theory (DFT) calculations^{18–25} so as to understand the fundamental mechanisms behind experimental observations. However, some questions are still unclear. For example, what are the roles of the organic molecule and inorganic matrix in photovoltaics, and what affects the electron pathway and transmission speed? To provide further insight into these questions, here, we perform DFT calculations with the inclusion of vdW correction for both the tetragonal and the orthorhombic phases of $\text{CH}_3\text{NH}_3\text{PbI}_3$ perovskites that have been well-observed in experiments.²⁶ Furthermore, the relation between structure and electronic and optical properties was fully investigated during phase change.

2. COMPUTATIONAL DETAILS

The DFT calculations were performed by applying the Vienna Ab initio Simulation Package (VASP) code.^{27,28} The electron–ion interaction was described by the projector augmented wave (PAW) method.^{29–31} Electronic orbitals 5d6s6p, 5s5p, 2s2p, 2s2p, and 1s were considered in valence for Pb, I, C, N, and H atoms, respectively. The basis set cutoff was 400 eV, and the k -space integration was done with a $4 \times 4 \times 4$ k -mesh in the Monkhorst–Park³² scheme. Further increasing the energy cutoff and k -points showed little difference in the results. All the structures considered in this study were relaxed with a conjugate-gradient algorithm until the energy on the atoms was less than 1.0×10^{-4} eV. Periodic boundary conditions were applied in all three dimensions. The cage made by four PbI_6

Received: May 20, 2014

Revised: August 7, 2014

Published: August 8, 2014

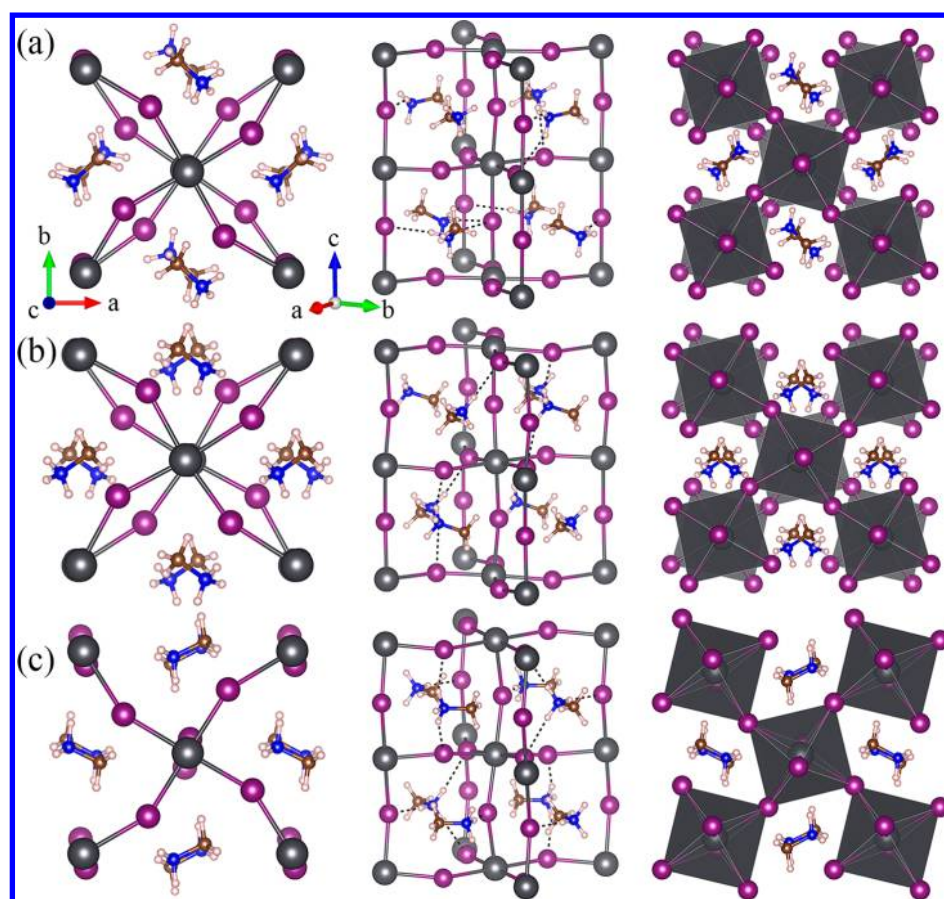


Figure 1. Optimized stable geometrical structures of (a) tet-p, (b) tet-v, and (c) ort phases. The left panel is a top view, the middle panel is a side view, and the right panel shows the structure in polyhedron graphs (dark gray: lead; purple: iodine; brown: carbon; blue: nitrogen; pink: hydrogen).

octahedron was rather large, and there was no obvious chemical bond formation between the organic molecule and the inorganic matrix. Therefore, a nonlocal density functional, vdW-DF,³³ was employed to take into account the weak interaction between them, as implemented in VASP by Klimeš et al.^{34,35} In this method, the exchange-correlation energy takes the form of

$$E_{xc} = E_x^{GGA} + E_c^{LDA} + E_c^{nl} \quad (1)$$

The semilocal GGA correlation such as the PBE correlation is replaced by the nonlocal form of the “vdW correlation” ($E_c^{LDA} + E_c^{nl}$) correlation energy). Here, the Perdew–Burke–Ernzerhof (PBE)³⁶ exchange functional was employed, along with the nonlocal vdW density functional, except as we noted below.

3. RESULTS AND DISCUSSION

3.1. Geometric Structures of $\text{CH}_3\text{NH}_3\text{PbI}_3$. $\text{CH}_3\text{NH}_3\text{PbI}_3$ has two typical crystal structures: the tetragonal (tet) phase at room temperature and the orthorhombic (ort) phase at low temperature (<162 K). In $\text{CH}_3\text{NH}_3\text{PbI}_3$, each Pb atom coordinates to six I atoms, with four I atoms in the equatorial direction and two I atoms in the apical direction. The four dipolar organic methylammonium ions (CH_3NH_3^+ , hereafter abbreviated as MA^+) are in the octahedron PbI_6 cages. Interestingly, the MA^+ ions in each unit cell of $\text{CH}_3\text{NH}_3\text{PbI}_3$ can have different distributions. For the orthorhombic phase, the C–N bonds in MA^+ are identified to distribute in a parallel way.³⁷ However, for the tetragonal phase, the orientation of the MA^+ ion is uncertain in the XRD experimental result, which

was attributed to the trigger of the transition.²⁶ In order to know the distribution effect on the structural stability, we started with several different initial orientations of MA^+ for tetragonal structures in this work.

The optimized configurations of different structures are shown in Figure 1, and the calculated cell parameters are listed in Table 1. The orthorhombic structure (denoted as “ort” in

Table 1. Calculated Relative Energies and Cell Parameters of $\text{CH}_3\text{NH}_3\text{PbI}_3$ for Both tet and ort Phases with PBE Combined with the Nonlocal Density Functional (vdW-DF). As for the tet, Both tet-p and tet-v Are Shown. The Corresponding Experimental Results Are Shown for Comparison

	rel. energy (eV)	this work (Å)			experiment (Å)		
		a	b	c	a	b	c
tet-p	0.37	8.94	8.94	12.98	8.80	8.80	12.69 ^a
tet-v	0.26	9.06	8.77	12.91			
ort	0	9.07	8.77	12.80	8.84	8.56	12.58 ^b

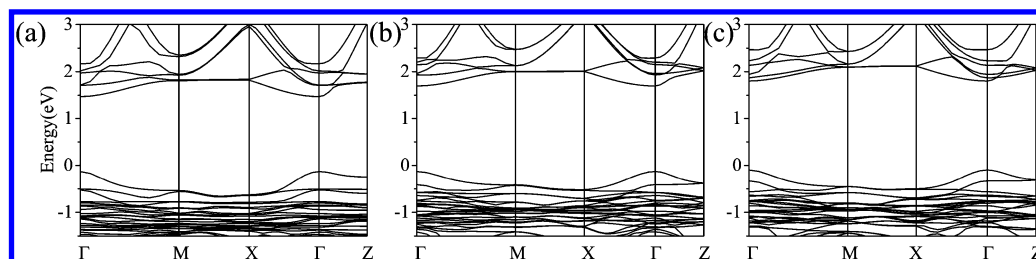
^aReference 26. ^bReference 37.

Figure 1c) is the most energetically stable one among the three structures, in good agreement with experiments where the $\text{CH}_3\text{NH}_3\text{PbI}_3$ presents in the orthorhombic structure at low temperature (<162 K).³⁷ The calculated cell parameters of the ort structure are 9.07, 8.77, and 12.80 Å, which are a little larger than the corresponding experimental values. The C–N bonds

Table 2. Calculated Bond Lengths of Pb–I, Bond Angles of Pb–I–Pb, and H Bond Number of CH₃NH₃PbI₃ for Both ort and tet Phases^a

	Pb–I bond length (Å)		Pb–I–Pb bond angle (deg)		H bond number
	equatorial	apical	equatorial	apical	
tet-p	3.20–3.29	3.21–3.28	151–160	168–179	6
tet-v	3.21–3.31	3.22–3.25	146–156	171–172	6
ort	3.26	3.26	150–152	157–159	12

^aThe H bond is determined by the distance between ammonium hydrogen atoms and iodine atoms, which should be smaller than 2.8 Å.

**Figure 2.** Calculated band structures for the different crystal structures of CH₃NH₃PbI₃: (a) tet-p, (b) tet-v, and (c) ort.

in MA⁺ distribute in a parallel way that is also consistent with experiments. We also examine to initially put MA⁺ in a vertical way, while they automatically recover to a parallel distribution after structure optimization. For the tetragonal phase, there are two typical distributions of MA⁺: one is that C–N bonds in MA⁺ distribute in a parallel way (tet-p, in Figure 1a), and the other is in the vertical way (tet-v, in Figure 1b). The tet-v is more thermodynamically stable than tet-p since the MA⁺ arrangement of tet-v can reduce the steric hindrance. The energy difference between tet-p and tet-v structures is small, about 0.11 eV, indicating the possible interconversion between them. This may be the reason that MA⁺ can move inside the cage at high temperatures in XRD and dielectric measurements.³⁸

The calculated Pb–I bond lengths and angles of the different structures are shown in Table 2. Interestingly, both the bond lengths and angles are greatly affected by the phase and the distribution of the MA⁺. For the ort structure, all the bond lengths of Pb–I are about 3.26 Å; thus, they are rather uniform. The corresponding Pb–I–Pb angles are 150–152° in the equatorial direction and 157–159° in the apical direction. When the structure changes from orthorhombic to tetragonal phase, PbI₆ octahedrons greatly rearrange, which leads Pb–I bonds to be nonuniform. The bond lengths of Pb–I are in a large range between 3.20 and 3.30 Å. The corresponding bond angles are in the range of 151–160° in the equatorial direction and 167–175° in the apical direction. The structure change leads to the expansion of parameter *c* for the tetragonal phase compared with the ort phase. The detailed tilting and distortion of PbI₆ octahedrons can be clearly seen in the polyhedron graphs (see Figure 1). The orthorhombic phase exhibits a coaxial octahedron rotation along the same direction, whereas the tetragonal phase staggers the rotation direction of octahedrons along the *c* axis.

It should be noted that the hydrogen bond (HB) also plays a vital role in the stability of the different structures. In this work, the hydrogen bond is defined by the bond length between ammonium hydrogen atoms and iodine atoms, with a value of <2.8 Å. The corresponding HBs are displayed as the dashed lines for the three structures. The ort structure contains 12 HBs, whereas the tet structures (tet-v and tet-p) have only 6 HBs. These HBs strengthen the interaction between the

organic molecule and the inorganic matrix and make the energy decrease, which might be the main reason why the ort structure is more stable.

We note that, in most of the previous theoretical studies, the lattice angles were constrained to be orthogonal during the structure optimization.^{25,39} To obtain real ground-state geometries, the atomic coordinates and cell parameters, including lattice angles, are fully optimized in this work. During the optimization of structures, the effect of dispersion interactions on the phase stability is also examined with the inclusion of vdW corrections. It was found that, when the dispersion interaction is not considered during the calculations, the calculated lattice angles are 91.3° for tet-p and 93.8° for tet-v. The corresponding cell lengths become 8.97, 8.94, and 13.14 Å for tet-p structures, which are 3.5% longer than experimental values. While considering the vdW interactions, the lattice angles remain at 90° without any constraints, and the lattice constants are 8.94, 8.94, and 12.98 Å for tet-p structures, more close to the experimental values.¹⁷ In previous theoretical works by Kim et al.,⁴⁰ the calculated cell parameters with PBE are 9.10, 9.02, and 12.77 Å for the tetragonal phase, and the corresponding volume is 1048.19 Å³. It is well-known that the PBE functional usually overestimates lattice constants for a wide variety of semiconductors, ionic solids, and metals.⁴¹ Our result slightly improves the volume to 1037.41 Å³; however, the result still overestimates the experimental lattice parameters. These results clearly suggest that the weak interactions between the organic and the inorganic moieties play an important role in determining the stability of CH₃NH₃PbI₃. Thus, the vdW correction is considered in the following calculations.

3.2. Electronic Properties. To provide further insight into the CH₃NH₃PbI₃ potential application in light harvesting, the electronic structures as crucial factors for DSC application are further explored. The calculated band structures of the three configurations are shown in Figure 2. Overall, the band structures of the three configurations are quite similar, which exhibit direct band gaps at the Γ point of the Brillouin zone. A slight difference could be seen for band dispersion along different directions. For the tet-p structure, the band structure (Figure 2a) of the valence band has a relatively large slope along Γ –M–X– Γ , but becomes relative flat along Γ –Z, which corresponds to the *c* axis. The calculated band gap is 1.60 eV,

in agreement with the available experimental result of 1.55 eV and the previous theoretical result of 1.63 eV.^{12,25} It is widely known that the GGA usually underestimates the band gap of semiconductors due to the self-correlation error of electrons and the inherent lack of derivative discontinuity. On the other hand, because of the presence of the heavy element Pb, the relativistic effects such as spin–orbit coupling, which is not considered here, would reduce the band gap. Therefore, the calculated band gap with GGA agrees with the experimental results due to the error cancellation. The conduction bands of tet-v and ort structures (see Figure 2b,c) are relatively higher than that of tet-p. The calculated band gaps of tet-v and ort structures are 1.82 and 1.90 eV, respectively, as listed in Table 3, indicating that the band gap of CH₃NH₃PbI₃ is greatly

Table 3. Calculated Band Gap and Effective Masses of CH₃NH₃PbI₃, Compared with the Other Results²¹

	band gap (eV)	effective mass			
		m_e^*	m_h^*	m_e^{*a}	m_h^{*a}
tet-p	1.60	0.18	0.28	0.19/0.17	0.25/0.28
tet-v	1.82	0.22	0.30		
ort	1.90	0.23	0.39		

^aEffective mass of tetragonal phase calculated by SOC-GW and SOC-DFT in ref 21.

affected by not only the phases but also the distribution of MA⁺. Overall, the ort phase possesses a relatively larger band gap than the tet phase. The calculated results clearly suggest that the interaction between MA⁺ and the inorganic matrix greatly affects the structure, which, in turn, changes the electronic structure of CH₃NH₃PbI₃.

Since the slope of the band edge is associated with the effective mass of the carrier, the electron transfer along *a* and *b* directions should be more favorable than that along the *c* direction. The effective charge carrier mass (m^*) of CH₃NH₃PbI₃ by fitting the band edge was calculated according to the following equation

$$m^* = \hbar^2 \left[\frac{\partial^2 \varepsilon(k)}{\partial k^2} \right]^{-1} \quad (2)$$

where $\varepsilon(k)$ is the band edge eigenvalues, and k is the wave vector. As shown in Table 3, m_e^* and m_h^* are 0.18 and 0.28 m_0 (m_0 is the electron static mass), respectively, for the tet-p structure. These results are quite close to the previous calculations for the tetragonal phase employing spin–orbit coupling (SOC) SOC-GW and SOC-DFT techniques.²¹ The effective masses of m_e^* and m_h^* are 0.22 and 0.30 m_0 for the tet-v structure and 0.23 and 0.39 m_0 for the ort structure, which are larger than those for the tet-p structure. Obviously, the

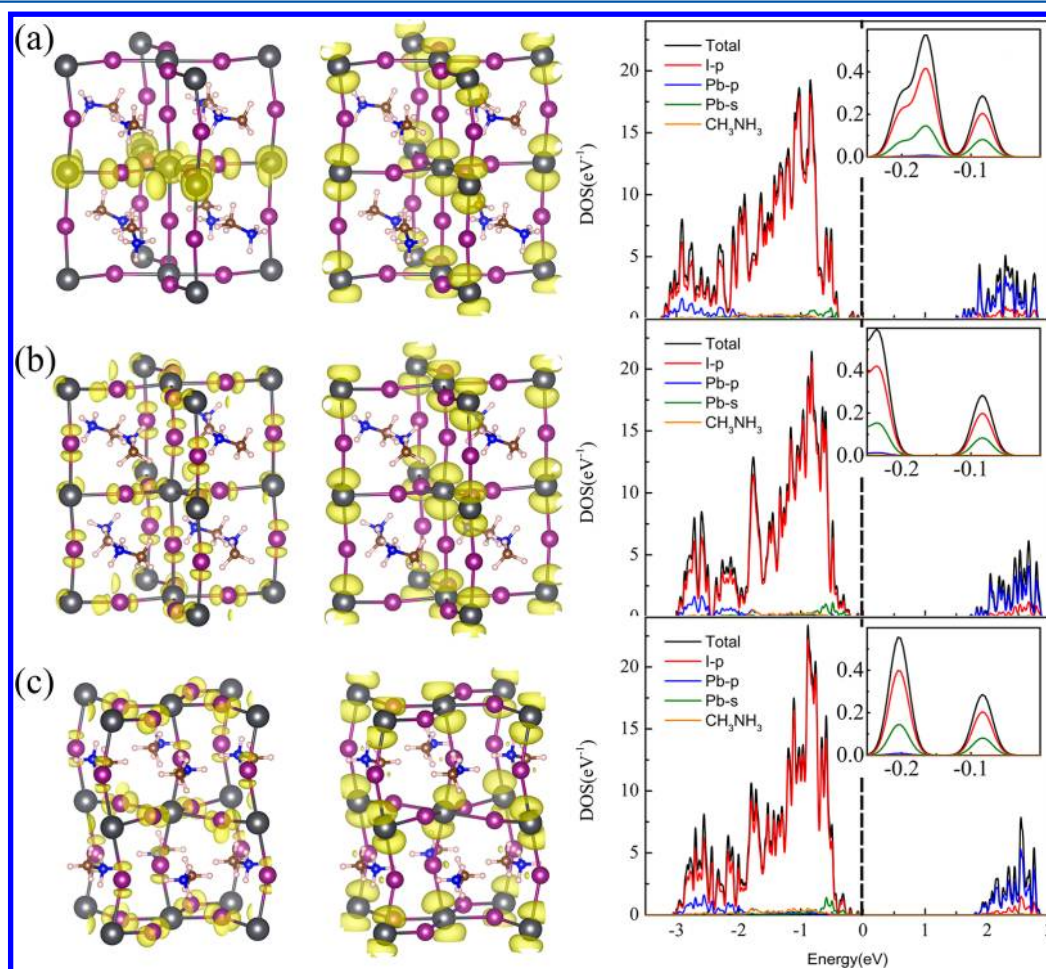


Figure 3. Left panel shows partial charge density plots for VBM (left) and CBM (right) of (a) tet-p, (b) tet-v, (c) ort. Right panel shows calculated PDOS, from top to bottom, for tet-p, tet-v, and ort structures; insets are enlargements of VBM (dark gray: lead; purple: iodine; brown: carbon; blue: nitrogen; pink: hydrogen).

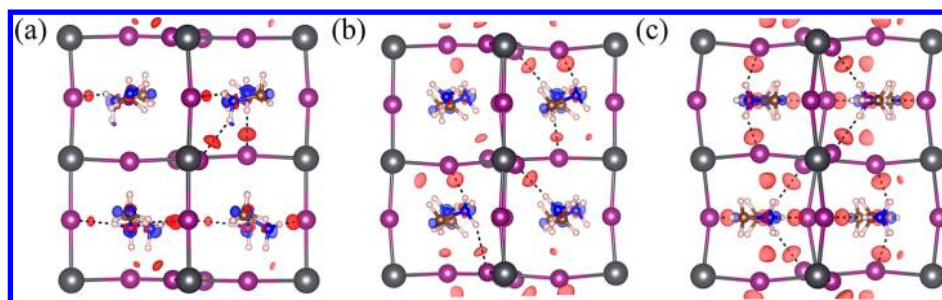


Figure 4. Charge density plots of (a) tet-p, (b) tet-v, and (c) ort structures (dark gray: lead; purple: iodine; brown: carbon; blue: nitrogen; pink: hydrogen).

effective mass is also changed by different structures. For all the studied structures, the calculated m_h^* values are larger than m_e^* values, and the carrier mobility of the tetragonal phase is a little higher than that of the ort phase.

In order to further understand the electronic structures of the three structures, the projected density of states (PDOS) and charge densities are analyzed. As shown in the right panel in Figure 3, the valence band maximum (VBM) for each system is mainly contributed by the p orbital of the I atom and partly contributed by the s orbital of the Pb atom, while the conduction band minimum (CBM) is dominated by p orbitals of the Pb atom. These features can also be seen in the partial charge densities of the CBM and VBM shown in the left panel in Figure 3. Yin et al.²⁴ studied the composition of the VBM and CBM and they found that the coupling between lone pair Pb-s orbitals and halogen-p orbitals played a key role in band structures and effective mass aspect. They considered that the strong s–p coupling led to the small effective mass of holes. Thus, our DFT results are well consistent with the previous theoretical results. Further, we note that the VBM of the ort and tet-v is distributed on all I atoms (Figure 3b,c), whereas the VBM of the tet-p structure is only distributed on the equatorial I atoms, barely on apical I atoms (Figure 3a). Such a difference should be the reason why the tet-p structure exhibits a relative flat band edge dispersion along the K-point path of Γ –Z.

Such results indicate that the CBM and VBM can effectively separate the electron and hole once upon the electrons on I-p and Pb-s (VBM) are excited to the Pb-p orbitals (CBM) under the light irradiation. The spatial distribution of the CBM and VBM can effectively enhance the lifetime of the electron and hole.

Since the CBM and VBM are contributed by I and Pb atoms, it is obvious that the band gap is greatly related to the Pb–I bond. As aforementioned, during the structural transformation from orthorhombic to tetragonal phase, the changes of the bond lengths become disordered, while the Pb–I–Pb bond angle increases regularly. The Pb–I–Pb bond angle also affects the distribution of the VBM. When the bond angle increases, both the VBM and the CBM turn from tilt to the Pb–I bond direction, which increases orbital overlapping between I and Pb. The enhanced interaction between I and Pb atoms could be responsible for the decrease of band gap.

On the other hand, both PDOS and partial charge density analyses show that MA^+ does not directly contribute electronic states in the band edge. However, the MA^+ indirectly affects the Pb–I bond by weak interaction. Figure 4 displays the charge density difference, i.e., the total density with the density of the isolated MA^+ and inorganic matrix subtracted. The red and blue colors represent charge accumulation and depletion, respec-

tively. It can be seen that the charge accumulation locates in the region between the I atom and the MA^+ matrix, as highlighted by the dashed line in Figure 4, which confirms the formation of a H–I hydrogen bond. There are obvious charge redistributions around the organic ions; thus, MA^+ also plays a vital role in the band gap by changing the Pb–I bond lengths. As discussed above, the ort structure contains more HBs than tet-v and tet-p structures. Therefore, Figure 4c displays more red color regions between MA^+ ions and the inorganic matrix, compared with tet-p and tet-v structures (see Figure 4a,b). Also, from the side view of Figure 4, one can see that the shapes of the PbI_6 cage for tet structures are different from that for the ort structure since the Pb–I–Pb angles increased.

3.3. Optical Properties. Besides the special electronic structure, $\text{CH}_3\text{NH}_3\text{PbI}_3$ also has excellent ability of light adsorption in the visible zone. The optical absorption coefficients of the three structures, calculated with the PBE functional along with vdW-DF, are shown in Figure 5.

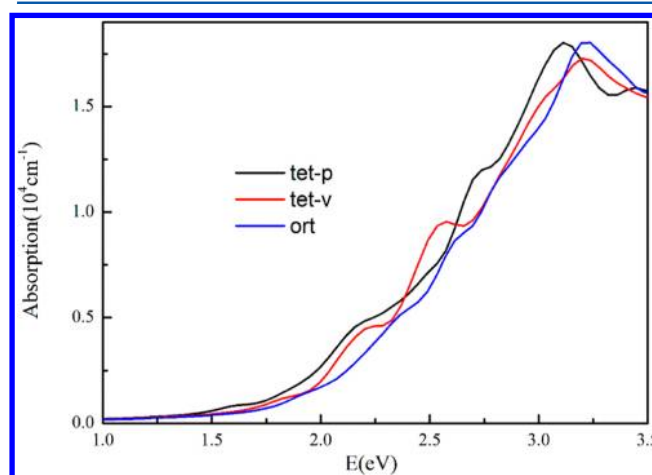


Figure 5. Calculated absorption coefficients of tet-p, tet-v, and ort with PBE along with vdW-DF, respectively.

The shapes of the three curves are quite close to each other, whereas the absorption coefficient curve moves to the red shift direction as the structure changes from ort to tet structure. The corresponding spectrum of the tet-v is slightly blue shifted than that of the tet-p structure. Such results agree with the trend of the band gap as discussed above. For example, the optical spectrum of the tet-p phase shows three peaks at about 1.65, 2.20, and 3.10 eV, corresponding to 750, 560, and 400 nm, respectively. Im et al.¹³ examined this system by UV–vis absorption spectra, and they reported three typical peaks at 420, 550, and 750 nm. They suggested that the high efficiency

of the perovskite sensitized solar cell is due to the large optical absorption at 550 nm, which is about an order of magnitude higher than that of N719 dye. Strikingly, the calculated positions of absorption peaks agree well with the experimental results. The first peak at about 1.65 eV is mainly due to the excitation from VBM to CBM. The second peaks at 2.20 eV might be because of transitions between the VB-1 to the CBM⁴². The absorption of MAPbI₃ in the visible light region is significantly intensive, which indicates that MAPbI₃ has superiority in utilizing solar energy. The intensive absorption of visible light for MAPbI₃ might be derived from the large and delocalized DOS around the CBM and small energy gaps of the direct optical transition points.

4. CONCLUSION

In summary, we have performed first-principles calculations to study the structural, electronic, and optical properties of the tetragonal and orthorhombic phases of CH₃NH₃PbI₃. The calculated results suggest that the distribution of methylammonium ions greatly affects both the stability and the electronic structure. The phase transition between orthorhombic to tetragonal phase is derived from the different torsion and arrangement of PbI₆ octahedrons. Interestingly, the phase transformation from orthorhombic to tetragonal phase decreases the band gap and the effective charge carrier mass. Further, the PDOS and partial charge densities reveal that the VBM is distributed by the p orbital of the I atom and partly contributed by the s orbital of the Pb atom and the CBM is distributed by p orbitals of the Pb atom, respectively. Thus, CH₃NH₃PbI₃ itself possesses the characteristic of unique electronic properties of spontaneous electron–hole separation. Although the organic molecules do not directly contribute to the band edge, they tune the electronic features by affecting the CH₃NH₃PbI₃ structure. The calculated optical spectra also suggest that CH₃NH₃PbI₃ is a promising material for optoelectronic applications because of the intensive optical absorption in the visible light region.

AUTHOR INFORMATION

Corresponding Author

*E-mail: limin.liu@csrc.ac.cn. Tel: +86-10-8268 7086 (L.-M.L.).

Notes

The authors declare no competing financial interest.

ACKNOWLEDGMENTS

This work was supported by the National Natural Science Foundation of China (No. 51222212), the CAEP Foundation (Grant No. 2012B0302052), and the MOST of China (973 Project, Grant No. 2011CB922200).

REFERENCES

- (1) O'Regan, B.; Grätzel, M.; Low-Cost, A. High-Efficiency Solar Cell Based on Dye-Sensitized Colloidal TiO₂ Films. *Nature* **1991**, *353*, 737–740.
- (2) Grätzel, M. Photoelectrochemical Cells. *Nature* **2001**, *414*, 338–344.
- (3) Liu, L.-M.; Li, S.-C.; Cheng, H.; Diebold, U.; Selloni, A. Growth and Organization of an Organic Molecular Monolayer on TiO₂: Catechol on Anatase (101). *J. Am. Chem. Soc.* **2011**, *133*, 7816–7823.
- (4) Nazeeruddin, M. K.; Kay, A.; Rodicio, I.; Humphry-Baker, R.; Mueller, E.; Liska, P.; Vlachopoulos, N.; Graetzel, M. Conversion of Light to Electricity by *cis*-X₂bis(2,2'-bipyridyl-4,4'-dicarboxylate)-

ruthenium(II) Charge-Transfer Sensitizers (X = Cl[−], Br[−], I[−], CN[−], and SCN[−]) on Nanocrystalline Titanium Dioxide Electrodes. *J. Am. Chem. Soc.* **1993**, *115*, 6382–6390.

(5) Sinke, W. C.; Wienk, M. M. Photochemistry: Solid-State Organic Solar Cells. *Nature* **1998**, *395*, 544–545.

(6) Nogueira, A. F.; Durrant, J. R.; De Paoli, M. A. Dye-Sensitized Nanocrystalline Solar Cells Employing a Polymer Electrolyte. *Adv. Mater.* **2001**, *13*, 826–830.

(7) Dualeh, A.; Delcamp, J. H.; Nazeeruddin, M. K.; Grätzel, M. Near-Infrared Sensitization of Solid-State Dye-Sensitized Solar Cells with a Squaraine Dye. *Appl. Phys. Lett.* **2012**, *100*, 173512.

(8) Mane, R. S.; Lee, W.; Min, S.-K.; Lee, S.-H.; Joo, O.-S.; Lokhande, C. D.; Shaikh, A. V.; Han, S.-H. Electrochemically Intercalated Indium-Tin-Oxide/Poly(3-Hexylthiophene): A Solid-State Heterojunction Solar Cell. *J. Chem. Phys.* **2009**, *130*, 111101.

(9) Park, N.-G. Organometal Perovskite Light Absorbers toward a 20% Efficiency Low-Cost Solid-State Mesoscopic Solar Cell. *J. Phys. Chem. Lett.* **2013**, *4*, 2423–2429.

(10) Wang, J. T.-W.; et al. Low-Temperature Processed Electron Collection Layers of Graphene/TiO₂ Nanocomposites in Thin Film Perovskite Solar Cells. *Nano Lett.* **2013**, *14*, 724–730.

(11) Gonzalez-Pedro, V.; Juarez-Perez, E. J.; Arsyad, W.-S.; Barea, E. M.; Fabregat-Santiago, F.; Mora-Sero, I.; Bisquert, J. General Working Principles of CH₃NH₃PbX₃ Perovskite Solar Cells. *Nano Lett.* **2014**, *14*, 888–893.

(12) Kojima, A.; Teshima, K.; Shirai, Y.; Miyasaka, T. Organometal Halide Perovskites as Visible-Light Sensitizers for Photovoltaic Cells. *J. Am. Chem. Soc.* **2009**, *131*, 6050–6051.

(13) Im, J.-H.; Lee, C.-R.; Lee, J.-W.; Park, S.-W.; Park, N.-G. 6.5% Efficient Perovskite Quantum-Dot-Sensitized Solar Cell. *Nanoscale* **2011**, *3*, 4088–4093.

(14) Chung, I.; Lee, B.; He, J.; Chang, R. P. H.; Kanatzidis, M. G. All-Solid-State Dye-Sensitized Solar Cells with High Efficiency. *Nature* **2012**, *485*, 486–489.

(15) Kim, H.-S.; et al. Lead Iodide Perovskite Sensitized All-Solid-State Submicron Thin Film Mesoscopic Solar Cell with Efficiency Exceeding 9%. *Sci. Rep.* **2012**, *2*, 591.

(16) Burschka, J.; Pellet, N.; Moon, S.-J.; Humphry-Baker, R.; Gao, P.; Nazeeruddin, M. K.; Grätzel, M. Sequential Deposition as a Route to High-Performance Perovskite-Sensitized Solar Cells. *Nature* **2013**, *499*, 316–319.

(17) Liu, M.; Johnston, M. B.; Snaith, H. J. Efficient Planar Heterojunction Perovskite Solar Cells by Vapour Deposition. *Nature* **2013**, *501*, 395–398.

(18) Even, J.; Pedesseau, L.; Jancu, J.-M.; Katan, C. Importance of Spin–Orbit Coupling in Hybrid Organic/Inorganic Perovskites for Photovoltaic Applications. *J. Phys. Chem. Lett.* **2013**, *4*, 2999–3005.

(19) Lang, L.; Yang, J.-H.; Liu, H.-R.; Xiang, H. J.; Gong, X. G. First-Principles Study on the Electronic and Optical Properties of Cubic ABX₃ Halide Perovskites. *Phys. Lett. A* **2014**, *378*, 290–293.

(20) Filippetti, A.; Mattoni, A. Hybrid Perovskites for Photovoltaics: Insights from First Principles. *Phys. Rev. B* **2014**, *89*, 125203.

(21) Umari, P.; Mosconi, E.; De Angelis, F. Relativistic GW Calculations on CH₃NH₃PbI₃ and CH₃NH₃SnI₃ Perovskites for Solar Cell Applications. *Sci. Rep.* **2014**, *4*, 4467.

(22) Amat, A.; Mosconi, E.; Ronca, E.; Quarti, C.; Umari, P.; Nazeeruddin, M. K.; Grätzel, M.; De Angelis, F. Cation-Induced Band-Gap Tuning in Organohalide Perovskites: Interplay of Spin–Orbit Coupling and Octahedra Tilting. *Nano Lett.* **2014**, *14*, 3608–3616.

(23) Yin, W.-J.; Shi, T.; Yan, Y. Unusual Defect Physics in CH₃NH₃PbI₃ Perovskite Solar Cell Absorber. *Appl. Phys. Lett.* **2014**, *104*, 063903.

(24) Yin, W.-J.; Shi, T.; Yan, Y. Unique Properties of Halide Perovskites as Possible Origins of the Superior Solar Cell Performance. *Adv. Mater.* **2014**, *26*, 4653–4658.

(25) Mosconi, E.; Amat, A.; Nazeeruddin, M. K.; Grätzel, M.; De Angelis, F. First-Principles Modeling of Mixed Halide Organometal Perovskites for Photovoltaic Applications. *J. Phys. Chem. C* **2013**, *117*, 13902–13913.

- (26) Kawamura, Y.; Mashiyama, H.; Hasebe, K. Structural Study on Cubic–Tetragonal Transition of $\text{CH}_3\text{NH}_3\text{PbI}_3$. *J. Phys. Soc. Jpn.* **2002**, *71*, 1694–1697.
- (27) Kresse, G.; Hafner, J. Ab Initio Molecular Dynamics for Liquid Metals. *Phys. Rev. B* **1993**, *47*, 558–561.
- (28) Kresse, G.; Furthmüller, J. Efficient Iterative Schemes for ab Initio Total-Energy Calculations Using a Plane-Wave Basis Set. *Phys. Rev. B* **1996**, *54*, 11169–11186.
- (29) Blöchl, P. E. Projector Augmented-Wave Method. *Phys. Rev. B* **1994**, *50*, 17953–17979.
- (30) Kresse, G.; Joubert, D. From Ultrasoft Pseudopotentials to the Projector Augmented-Wave Method. *Phys. Rev. B* **1999**, *59*, 1758–1775.
- (31) Blöchl, P.; Först, C.; Schimpl, J. Projector Augmented Wave Method: Ab Initio Molecular Dynamics with Full Wave Functions. *Bull. Mater. Sci.* **2003**, *26*, 33–41.
- (32) Monkhorst, H. J.; Pack, J. D. Special Points for Brillouin-Zone Integrations. *Phys. Rev. B* **1976**, *13*, 5188–5192.
- (33) Dion, M.; Rydberg, H.; Schröder, E.; Langreth, D. C.; Lundqvist, B. I. Van Der Waals Density Functional for General Geometries. *Phys. Rev. Lett.* **2004**, *92*, 246401.
- (34) Klimeš, J.; Bowler, D. R.; Michaelides, A. Chemical Accuracy for the van der Waals Density Functional. *J. Phys.: Condens. Matter* **2010**, *22*, 022201.
- (35) Klimeš, J.; Bowler, D. R.; Michaelides, A. van der Waals Density Functionals Applied to Solids. *Phys. Rev. B* **2011**, *83*, 195131.
- (36) Perdew, J. P.; Burke, K.; Ernzerhof, M. Generalized Gradient Approximation Made Simple. *Phys. Rev. Lett.* **1996**, *77*, 3865–3868.
- (37) Baikie, T.; Fang, Y.; Kadro, J. M.; Schreyer, M.; Wei, F.; Mhaisalkar, S. G.; Grätzel, M.; White, T. J. Synthesis and Crystal Chemistry of the Hybrid Perovskite $(\text{CH}_3\text{NH}_3)\text{PbI}_3$ for Solid-State Sensitised Solar Cell Applications. *J. Mater. Chem. A* **2013**, *1*, 5628–5641.
- (38) Poglitsch, A.; Weber, D. Dynamic Disorder in Methylammoniumtrihalogenoplumbates (II) Observed by Millimeter-Wave Spectroscopy. *J. Chem. Phys.* **1987**, *87*, 6373–6378.
- (39) Quarti, C.; Grancini, G.; Mosconi, E.; Bruno, P.; Ball, J. M.; Lee, M. M.; Snaith, H. J.; Petrozza, A.; Angelis, F. D. The Raman Spectrum of the $\text{CH}_3\text{NH}_3\text{PbI}_3$ Hybrid Perovskite: Interplay of Theory and Experiment. *J. Phys. Chem. Lett.* **2013**, *5*, 279–284.
- (40) Kim, J.; Lee, S.-H.; Lee, J. H.; Hong, K.-H. The Role of Intrinsic Defects in Methylammonium Lead Iodide Perovskite. *J. Phys. Chem. Lett.* **2014**, *5*, 1312–1317.
- (41) Perdew, J. P.; Ruzsinszky, A.; Csonka, G. I.; Vydrov, O. A.; Scuseria, G. E.; Constantin, L. A.; Zhou, X.; Burke, K. Restoring the Density-Gradient Expansion for Exchange in Solids and Surfaces. *Phys. Rev. Lett.* **2008**, *100*, 136406.
- (42) Xing, G.; Mathews, N.; Sun, S.; Lim, S. S.; Lam, Y. M.; Grätzel, M.; Mhaisalkar, S.; Sum, T. C. Long-Range Balanced Electron- and Hole-Transport Lengths in Organic-Inorganic $\text{CH}_3\text{NH}_3\text{PbI}_3$. *Science* **2013**, *342*, 344–347.